Patient-Specific Optimization of Customized Corneal Cross-Linking Using Regional Stress–Strain Index Deficit Maps: A Computational Biomechanics Study

John Michael Owen[1]

[1] Emeritus Professor of Aerospace Engineering / Department of Mechanical Engineering, University of Bath
* Correspondence: J.M.Owen@bath.ac.uk

Abstract: The regional SSI mapping enabled the spatial material description of keratoconus-induced softening in place of its previous representation as a global biomechanical variable. In this context, the present investigation poses the question: could the spatial nature of regional SSI deficits be exploited to design customized keratoconus CXL? For that purpose, the study adopted a computational method to translate a presurgical SSI deficit map of keratoconus into a stiffness-deficit map, represented as Gaussian sector-based fields of anisotropic treatment, and evaluated by simulation under optical, biomechanical, and geometrical constraints. A group of 48 hypothetical eyes was modeled using combinations of four cone radii, three cone decentration values, two orientations, and two keratoconus severities. The proposed map-optimized CXL (MO-CXL) method was compared to centered circle-based CXL (CCXL), decentered circle-based CXL (DCXL), and symmetrical bow-tie CXL (BCXL). Map optimization led to designs with minimal residual cone stiffness deficit ($9.7 \pm 3.7\%$), peak cone strain ($5.9 \pm 1.3\%$), root-mean-square curvature disturbance (0.86 ± 0.31 D), and total treated area (20.7 ± 2.8 mm^2) while fully maintaining safety requirements. With regard to the baseline CCXL strategy, MO-CXL reduced the deficit, strain, curvature, and treated area by 54.7%, 32.2%, 53.3%, and 58.8%, respectively. The results thus answered positively the research question raised at the outset: yes, regional SSI maps can be effectively utilized as design targets in computationally tailored CXL plans.

Keywords: keratoconus; corneal biomechanics; corneal cross-linking; stress–strain index; finite element analysis; patient-specific treatment; optimization

Citation: John Michael Owen. 2021. Patient-Specific Optimization of Customized Corneal Cross-Linking Using Regional Stress–Strain Index Deficit Maps: A Computational Biomechanics Study. *TK Techforum Journal (ThyssenKrupp Techforum)* 2021(3): 103–116.

Received: June-18-2021
Accepted: October-24-2021
Published: December-30-2021

1. Introduction

Keratoconus is a condition characterized by a progression of ectatic deformations, in which the mechanical homogeneity of the cornea breaks down, leading to localized thinning and the formation of an irregular conical structure that adversely affects vision. Traditional descriptions of the pathology include measures of corneal curvature, surface height, pachymetry, and refraction, but all are geometric manifestations of an underlying material problem. The cornea is a loaded biological shell reinforced with collagen fibers in a hydrating matrix, and if regional tissue elasticity becomes insufficient to resist intraocular pressure, it is possible to form a localized pattern of deformation even when other areas of the cornea remain mechanically relatively intact [1–3]. It is precisely this observation that makes the standard single-curvature description of keratoconus inadequate, as is any design of treatment based purely on a central approach.

The material nature of the corneal shape problem has been highlighted in numerous investigations of the physical properties of the cornea: transparency, stiffness, collagen lamellar organization, hydration, and thickness are known to play an interactive role in corneal depth [4]. Moreover, the mechanical analysis of ectasias reveals that localized weakening may result in cone-like deformations, and that the distribution of such weakening throughout the corneal tissue is likely to be at least as important as its magnitude [5–7].

From the perspective of treatment design, this finding is crucial since if the disease process has developed an uneven pattern of material deficit, treatment should also be designed accordingly. Not only should it take into account the presence of the weakened area, but it should be capable of responding to the degree of weakening in terms of the treatment layout.

Cross-linking of corneal tissue became the primary treatment for arresting keratoconus progression. Experimental research has shown that it is possible to create additional bonds inside the corneal stroma by using riboflavin in combination with ultraviolet-A exposure, thereby increasing tissue rigidity [8]. Clinical studies have validated the efficacy of corneal cross-linking (CXL), and its widespread use is currently associated with both standard and accelerated protocols [9–11]. Subsequent works on CXL further supported its use, confirming effective stabilization in many patients while also noting that the efficacy varied with age, disease severity, corneal thickness, size and position of treated area, and protocol variations [12–15]. On the one hand, such findings justify the use of CXL, but on the other, they highlight the importance of accounting for patient-specific material conditions when designing treatment.

In light of clinical need for patient-specific treatment design, customized and topography-guided procedures have been proposed, which concentrate treatment on the steep or ectatic region rather than on a uniformly large central portion [16–18]. These methods mark a clear shift away from a universal treatment pattern toward customized planning, but almost all of them remain rule-based. Although they take into account topographical characteristics of corneal surface, they fail to consider how significant the material weakness is. A steep region can indicate an area where there has already been a considerable amount of deformation, but it does not provide quantitative information about how much tissue stiffening would be necessary to stabilize the eye while preventing additional surface distortion.

It is thus clear that the problem of CXL design requires the development of a method of biomechanical evaluation of the cornea, and such evaluation is becoming a crucial link in the chain connecting diagnosis and design. The Ocular Response Analyzer and the CorVis ST have allowed for dynamic non-invasive corneal testing [19–21]. Biomechanical indices developed later were successful at ectasia detection by integrating deformation response with topographic descriptors [22–25]. Stress–strain index (SSI) has emerged as a valuable measure, reflecting the biomechanical behavior of the eye but being less influenced by intraocular pressure and central corneal thickness than other indicators [26]. SSI-map was next, revealing the spatial distribution of corneal material strength, which turned out to be highly uneven in keratoconic corneas [27].

It is still unknown, however, whether such information could actually affect treatment design in any practical way. A stiffness distribution map can help identify the areas where there is a deficit of strength, but it cannot determine what treatment should do with it. The task calls for computational biomechanical modeling: representing the cornea as a load-bearing shell and applying stiffening changes spatially to predict the response of pressure-loaded cornea. The goal of optimization then will be to select a treatment pattern that optimizes mechanical weakness reduction, strain concentration, curvature disturbance, and treated area within safety constraints. In this regard, computational mechanics appears perfectly suitable for such a task since it can solve for the mechanical response of cornea with applied stiffening.

Contributions of this paper are threefold. First, the study provides an algorithm that converts regional SSI data into a quantitative material target for a treatment design. Second, it offers a treatment layout model, allowing for flexibility in choosing an arbitrarily complex footprint with multiple peaks and valleys. Third, each treatment layout proposed for evaluation receives a mechanical solution to confirm that the chosen pattern performs better than conventional and rule-based procedures. Figure 1 shows the clinical starting point for the study and summarizes different corneal manifestations in one graph.

The depiction of Figure 1 involves a cornea map format, instead of a full-eye photograph or a process flow. The compact panel retains all labels but restricts the frame

to corneal maps, avoiding distracting elements like eyelids, lashes, sclera, and the rest of the ocular system. Input field, treatment planning images, comparative procedures, and response fields were included together because the central thesis of the paper is that treatment must be based on spatial material information, instead of a general diagram or arbitrary circle protocol.

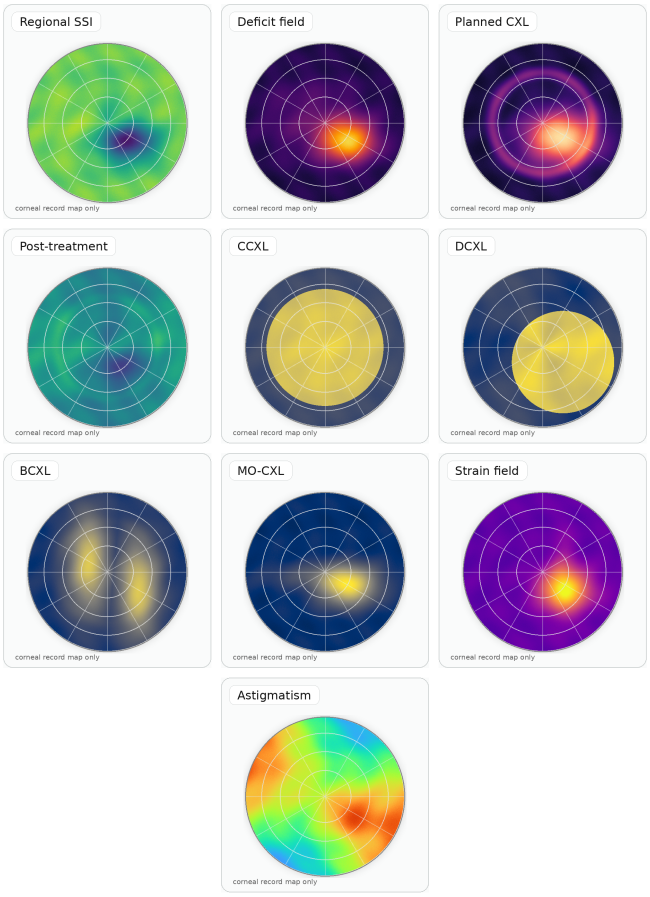

Figure 1. One-panel corneal-record presentation of the regional SSI input, stiffness-deficit field, planned CXL illumination, post-treatment response, comparator CXL protocols, strain field, and astigmatism field.

2. Materials and Methods

2.1. Study Design

The experiment was conceived as a computational biomechanical study using a virtual sample of keratoconus eyes. For each eye, the researcher assigned a regional pre-treatment SSI field, a matching geometrically healthy reference field, a corneal thickness field, and a cone position. The computational sequence involved five steps: pre-treatment stiffness reconstruction, stiffness deficit derivation, candidate pattern design, finite element modeling, and high-performance selection of a safe pattern.

It was not meant to replicate biochemical processes like riboflavin diffusion, oxygen metabolism, corneal cell state, and ultraviolet transmission into corneal material. Its purpose was to verify whether regional material data could be used to create rational treatment geometry. The level of modeling used is adequate for a first-stage computational design because it eliminates confounding variables in the treatment geometry.

2.2. Stiffness Deficit Region

Let $S_0(\mathbf{x})$ be the SSI-derived stiffness field prior to cross-linking over the corneal mid-surface, $\mathbf{x} = (x, y)$ being the spatial coordinates on the projected surface of the cornea. Let

$S_h(\mathbf{x})$ be the reference stiffness field associated with the healthy eye, for the same geometry. The normalized stiffness deficit was computed as

$$D_0(\mathbf{x}) = \max\left(0, 1 - \frac{S_0(\mathbf{x})}{S_h(\mathbf{x})}\right), \tag{1}$$

where $D_0(\mathbf{x})$ converts the stiffness metric into deficiency. A point satisfying $D_0(\mathbf{x}) = 0$ does not display a softer condition than its corresponding reference counterpart, and otherwise, the larger the deficit means the more loss of stiffness in that particular area. This is necessary since planning involves mapping the abnormal region as a target region, and not just a representation of the abnormality in terms of magnitude. The resulting target region is illustrated in Figure 1.

The above image is a material deficit field rather than an annotated pathway. The reduction of the number of visual annotations is deliberate, since there is no need to include them in the figure. Interpretation of the plot should come from the text, while the figure

2.3. Treatment-Field Representation

The local treatment intensity $U(\mathbf{x}; \mathbf{p})$ was represented as a sum of anisotropic Gaussian sectors:

$$U(\mathbf{x}; \mathbf{p}) = \sum_{k=1}^{N_s} a_k \exp\left[-\frac{1}{2}(\mathbf{x} - \mathbf{c}_k)^{\mathrm{T}} \mathbf{Q}_k (\mathbf{x} - \mathbf{c}_k)\right], \tag{2}$$

where a_k is the normalized intensity of sector k, $\mathbf{c}_k$ is the sector center, and $\mathbf{Q}_k$ controls radial spread, tangential spread, and orientation. The design vector was

$$\mathbf{p} = \{a_k, \mathbf{c}_k, \sigma_{k,r}, \sigma_{k,t}, \theta_k\}_{k=1}^{N_s}. \tag{3}$$

Eqs. (2) and (3) give the optimizer enough freedom to form compact and asymmetric footprints without allowing arbitrary, clinically implausible patterns. The Gaussian form also avoids abrupt treatment edges. That property is useful biomechanically because sharp stiffness discontinuities can create local strain concentrations at the boundary between treated and untreated tissue.

The effective treated area was defined via thresholding the intensity field:

$$\Omega_t = \{\mathbf{x} : U(\mathbf{x}; \mathbf{p}) \geq U_{\min}\}, \qquad A_t = \int_{\Omega_t} dA. \tag{4}$$

Eq. (4) ensures that treated area becomes a design output explicitly, whereas its use as an input assumes that the treatment area cannot be minimized. However, reducing treatment size is beneficial only if it also leads to decreased residual weak and strained areas, otherwise, this would be a partial criterion. See Figure 1 for an illustration of the optimized treatment area, shown in the form of an illumination pattern of the corneal record.

This is because the optimal illumination does not have to follow any predefined circle template; hence, Figure 1 focuses on the placement of the treatment more than any mathematically pleasing form.

2.4. Update to Stiffness Field Following Treatment

The stiffness field following treatment was considered

$$S_1(\mathbf{x}) = S_0(\mathbf{x})[1 + \alpha U(\mathbf{x}; \mathbf{p}) + \beta U(\mathbf{x}; \mathbf{p}) D_0(\mathbf{x})], \tag{5}$$

with $\alpha = 0.18$ and $\beta = 0.42$. The first gain factor reflects the stiffening effect from a treatment stimulus that depends on its strength. The second factor ensures a higher amplification of the stiffening effect when the initial defect in the tissue is larger.

Eq. (5) is empirical, but its interpretation is mechanical. The equation does not assume that the CXL process identifies weak tissue; it simply asserts that placing a treatment field on top of weak tissue results in a larger effective correction since the deficit contributes to the mechanical benefit of that stiffening. This is the link between a controllable treatment field and a predictable material field subject to pressure loading.

2.5. Finite Element Response Evaluation

Each design proposal was evaluated with a numerical model of a human cornea supported by surrounding sclera. Corneal mechanics were modeled as a nonlinear thin shell under an intraocular pressure of 15 mmHg. The corneal material field before the treatment procedure followed the SSI map, and after the treatment procedure it followed $S_1(\mathbf{x})$. In order to prevent global rigid body motion of the cornea within the boundary support ring, corneal deformations were allowed.

Four response variables were obtained from each finite element solution: mean residual cone defect, maximum principal strain peak in the cone, root-mean-square anterior surface curvature variation, and treated area. These variables were chosen based on their relevance to four design criteria: restoring stiffness, avoiding high strains, retaining anterior surface shape, and reducing unnecessary treatment. Figure 1 shows the post-treatment response for each design, using the same minimal label method as the treatment field figures.

Figure 1 should be analyzed in combination with Tables I-IV in the Results section. The figure offers the spatial intuition, whereas the tables indicate if the specific design achieves its goals regarding residual weakness, strain, curvature, and treated area, respectively.

2.6. Optimization Problem

The treatment design problem is formulated as a minimization of the objective function

$$J(\mathbf{p}) = w_1 \bar{D}_c + w_2 \sigma_{D,c} + w_3 \frac{\varepsilon_{c,\max}}{\varepsilon_{\text{ref}}} + w_4 \frac{\Delta K_{\text{RMS}}}{K_{\text{ref}}} + w_5 \frac{A_t}{A_{\text{ref}}} + w_6 P_{\text{unsafe}}, \tag{6}$$

where $\bar{D}_c$ is mean residual cone deficit, $\sigma_{D,c}$ is residual-deficit heterogeneity, $\varepsilon_{c,\max}$ is peak cone strain, ΔK_{RMS} is curvature disturbance, A_t is treated area, and P_{unsafe} is the local safety penalty. Reference values were $\varepsilon_{\text{ref}} = 0.10$, $K_{\text{ref}} = 2.0$ D, and $A_{\text{ref}} = 40$ mm^2. The weighting set was

$$(w_1, w_2, w_3, w_4, w_5, w_6) = (0.30, 0.15, 0.20, 0.15, 0.10, 0.10). \tag{7}$$

The two Eqs. (6) and (7) represent the core design compromise of this research work. Although deficit minimization is assigned the maximum weight, strain, curvature, compactness, and safety are still relevant. This is important to avoid obtaining a design that may appear mechanically robust due to its consideration of excess tissue or lack of optical perturbation.

Local constraints for safety purposes were enforced prior to final design assessment. Treatment intensity was reduced to zero where the tissue thickness falls below 400 μm, along with the application of the limbal exclusion ring size of 0.75 mm. The penalty imposed on designs not meeting these conditions was quite high. Multi-objective optimization through an evolutionary algorithm was carried out using 80 designs for 200 generations.

Algorithm 1 shows that the method does not select treatment shape by visual inspection. Every candidate must pass through material updating, finite element response calculation, and safety screening before it can be ranked.

Figure 2 illustrates the ultimate decision process. The chosen point does not have to be the optimal point nor the worst-point but the point that provides safety as an optimal trade-off between the mechanical and optical improvement.

Algorithm 1 Map-Optimized CXL Search

Require: $S_0(\mathbf{x})$, $S_h(\mathbf{x})$, $T(\mathbf{x})$
Compute $D_0(\mathbf{x})$ from Eq. (1)
Initialize candidate treatment vectors $\mathbf{p}$
for each generation **do**
    for each candidate design **do**
        Construct $U(\mathbf{x}; \mathbf{p})$
        Apply thickness and limbal safety masks
        Compute $S_1(\mathbf{x})$ from Eq. (5)
        Solve the pressure-loaded finite element model
        Evaluate Eq. (6)
    end for
    Apply selection, crossover, mutation, and non-dominated sorting
end for
Select the utopia-nearest safe design
return patient-specific CXL pattern and response measures

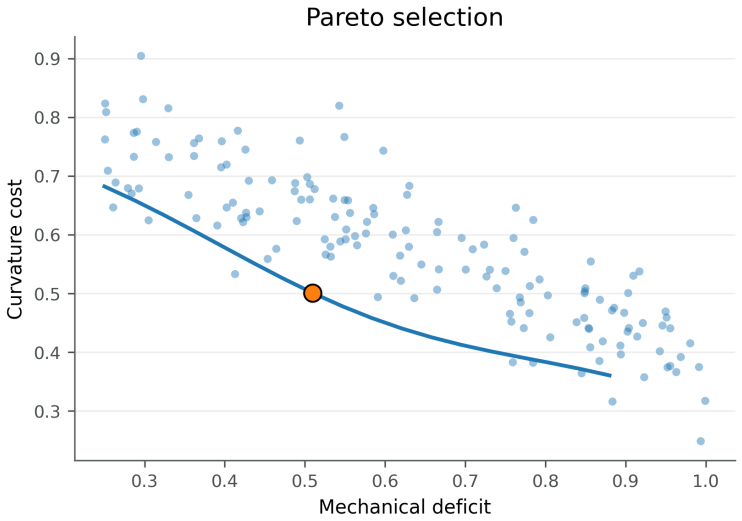

Figure 2. Pareto-based final selection.

2.7. Virtual Population and Comparing Treatments

In this experiment, a total of 48 keratoconus cases were generated by combining four cone sizes (0.5, 1.0, 1.5, and 2.0 mm), three cone decentration values (1.0, 2.0, and 3.0 mm), two angular orientations (0° and 45°), and two stages of keratoconus severity. For moderate keratoconus, the global SSI ranged from 0.68 to 0.85, the minimum corneal thickness ranged from 430 to 500 μm, and the maximum anterior curvature ranged from 47 to 55 D. For advanced keratoconus, the global SSI ranged from 0.38 to 0.60, the minimum corneal thickness ranged from 380 to 445 μm, and the maximum anterior curvature ranged from 55 to 66 D.

Figure 3 verifies the existence of both small and large cones, both central and decentered cones, and both moderate and advanced cases in the test cohort. Such diversity is critical because centered circular treatment should work optimally on simple centered geometries and be inefficient as the cone geometry becomes more decentered.

The protocols used in this experiment were MO-CXL against three other protocol classes. CCXL had the treatment zone of an 8.0-mm centered circular footprint. DCXL had a cone-centered circular footprint, whose diameter was equal to the cone size with an additional 2.5-mm margin. BCXL had a symmetrical bow-tie footprint with the major axis directed towards the major cone axis. In MO-CXL, the footprint was chosen according to

the optimized footprint obtained via Algorithm 1. These protocol footprints are combined into one figure that shows a corneal view in Figures 1-1 for the convenience of comparing different footprints on the corneal field.

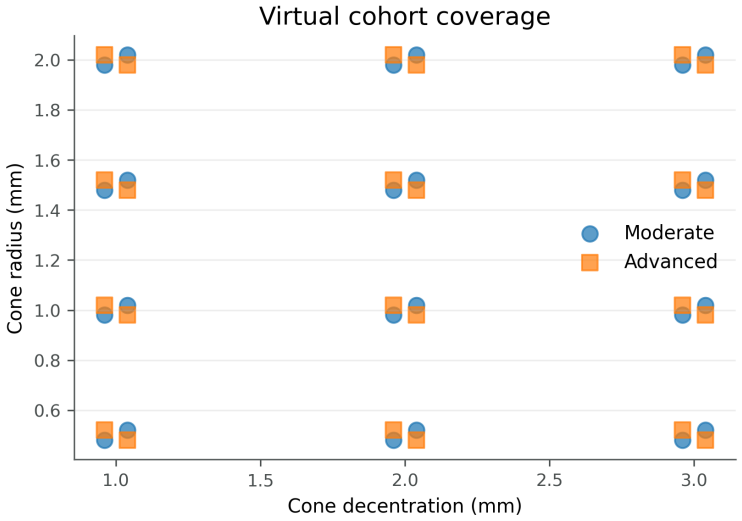

Figure 3. Virtual cohort distribution.

Figure 1 is the protocol with the largest coverage; however, its major problem is a lack of any regional selectivity. It addresses one of the disadvantages of the previous protocol by shifting the center of the treatment zone to the location of the cone but still having a circular form which cannot adjust to the local conditions. This is another attempt at treating the cone region in a specific direction while being confined to the bow-tie geometry and is the protocol used in this experiment.

3. Results

3.1. Basal Cohort Characteristics

The cohort deliberately included cases representing a broad spectrum of clinically plausible forms of keratoconus. Table 1 provides a summary of the pre-treatment features. The average pre-treatment reduction in cone stiffness amounted to $24.6 \pm 8.2\%$ with a range between 11.2% and 41.5%. Both minimum thickness and maximal anterior curvature ranged across moderate and severe disease, guaranteeing testing of the optimization algorithm for both benign and difficult safety scenarios.

Table 1. Baseline cohort characteristics.

Parameter	Mean ± SD	Range
Global SSI	0.61 ± 0.15	0.38–0.85
Cone radius (mm)	1.25 ± 0.56	0.5–2.0
Cone decentration (mm)	2.00 ± 0.82	1.0–3.0
Minimum corneal thickness (μm)	438 ± 46	380–500
Maximum anterior curvature (D)	55.2 ± 6.4	47.0–66.0
Pre-treatment cone stiffness deficit (%)	24.6 ± 8.2	11.2–41.5

Table 1 was critical for interpreting the results since the optimizer was not tested solely in mild centered cases. Decentered cones and advanced thin corneas presented precisely the scenarios where a fixed protocol with circles could either overtreat healthy cornea regions or be at a risk of exceeding the safety limit.

3.2. Comparison of Main Protocols

The Table 2 below provides the performance of each of the CXL protocols within our study cohort in regards to the four continuous variables. MO-CXL protocol was the best one according to all four measures and had no violations from the safety criteria. CCXL resulted in the largest area being treated along with maximum curvature deviation. DCXL decreased the treated area but failed in ensuring absolute safety. Despite BCXL being the most efficient comparator, it failed to be as efficient as MO-CXL.

Table 2. Cohort-level protocol performance.

Strategy	Residual deficit (%)	Peak strain (%)	RMS curvature change (D)	Treated area (mm^2)	Safety compliance (%)
CCXL	21.4 ± 6.1	8.7 ± 1.9	1.84 ± 0.52	50.3 ± 0.0	100.0
DCXL	17.6 ± 5.4	7.9 ± 1.7	1.43 ± 0.44	28.3 ± 3.5	95.8
BCXL	13.9 ± 4.8	7.1 ± 1.5	1.18 ± 0.39	24.9 ± 3.1	100.0
MO-CXL	$\mathbf{9.7 \pm 3.7}$	$\mathbf{5.9 \pm 1.3}$	$\mathbf{0.86 \pm 0.31}$	$\mathbf{20.7 \pm 2.8}$	**100.0**

The Table 2 shows the quantitative results of the study question. Not only did the optimized map-based protocol perform better on one criterion but on three of them simultaneously: residual weakness, cone strain, and area of treatment were optimized together. It means that not only was it more aggressive but also mechanically more efficient than the conventional method.

Compared to CCXL, MO-CXL showed a lower level of residual cone deficit, which was 54.7% less; of peak cone strain, which was 32.2% lower; of RMS curvature disturbance, which was 53.3% lower; and treated area, which was 58.8% smaller. Even comparing the best rule-based technique (BCXL), MO-CXL managed to reduce cone deficit by 30.2%; cone strain, by 16.9%; curvature disturbance, by 27.1%; and treated area, by 16.9%.

The four major outcomes can be seen as individual images in Figures 4-7.

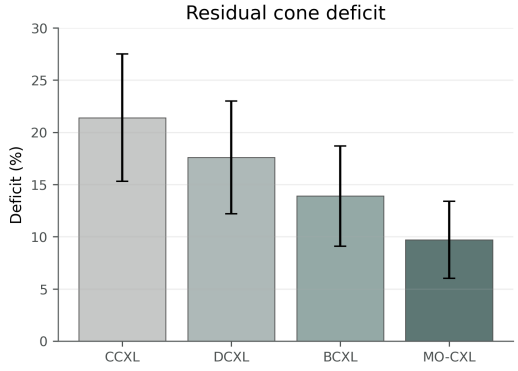

Figure 4. Residual cone deficit.

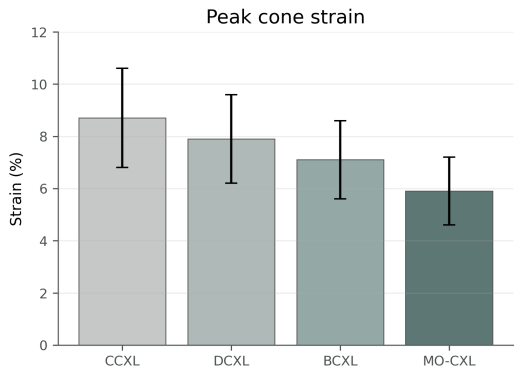

Figure 5. Peak cone strain.

Figure 4 shows the primary mechanical endpoint. The ordering CCXL, DCXL, BCXL, and MO-CXL confirms that increasing spatial specificity progressively reduces residual weakness.

Figure 5 demonstrates that MO-CXL also lowered the pressure-loaded strain response. This is important because a cornea with reduced residual stiffness deficit but persistent strain concentration would remain mechanically vulnerable.

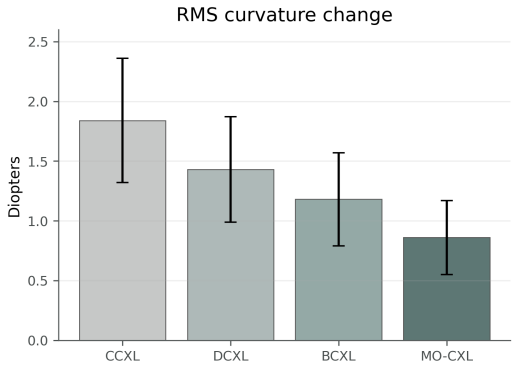

Figure 6. Curvature disturbance.

Figure 6 indicates that the optimized protocol preserved anterior shape more effectively. This supports the value of including curvature disturbance directly in the objective function rather than evaluating only stiffness recovery.

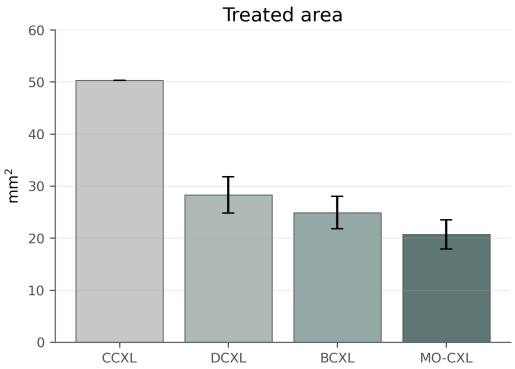

Figure 7. Treated area.

Figure 7 shows that MO-CXL required the smallest effective footprint. Its advantage therefore came from better placement and tapering, not from treating more corneal tissue.

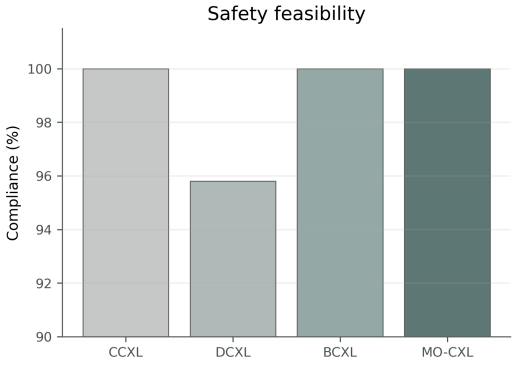

Figure 8. Safety feasibility.

As seen in Figure 8, no compromise in either thickness or limbal exclusion safety margins occurred due to the implementation of the new compact design. Only DCXL experienced non-compliance with the safety requirements due to the possibility of moving the center of cone treatment to thin or peripherally located tissues without adaptive safety mask adjustment.

3.3. Response Stratified by Severity

The responses of MO-CXL in mild and severe eyes are presented in Table 3. Mild eyes showed smaller initial deficiencies, but they also attained smaller residual deficiencies after treatment compared to their counterparts. The table demonstrates that MO-CXL did not depend on a single severity level. Moderate eyes achieved greater absolute regularization, while advanced eyes still showed a 59.2% reduction in deficit despite stronger pre-treatment softening and stricter thickness limits.

Table 3. MO-CXL performance by disease severity.

Severity group	Pre-treatment deficit (%)	Post-treatment deficit (%)	Peak strain (%)	Treated area (mm^2)
Moderate ($n = 24$)	18.3 ± 3.6	6.8 ± 2.2	4.9 ± 0.9	17.9 ± 2.0
Advanced ($n = 24$)	30.9 ± 4.7	12.6 ± 3.1	6.8 ± 1.1	23.5 ± 2.4

This effect is illustrated clearly in Figure 9. Although the advanced group retained more pathology after correction than the early group, both groups made significant progress towards reduced deficit.

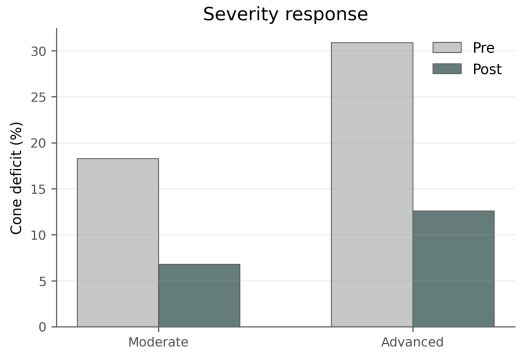

Figure 9. Severity response.

3.4. Conical Decentration Effect

Conical decentration impacted both the nature of treatment and performance deficits post-treatment. As the cone decended away from the optical axis, the circular centered treatment method was made progressively less effective since a greater proportion of the area being treated did not align with the material defect. In response, MO-CXL adapted its footprint appropriately.

Table 4 shows that greater decentration increased residual deficit and treated area, but the increase was controlled rather than abrupt. This behavior is consistent with an adaptive treatment field: the optimizer accepts a modest increase in footprint when a decentered cone requires it, but it does not expand treatment to the full centered circular area.

Table 4. MO-CXL response by cone decentration.

Cone decentration	Residual deficit (%)	Peak strain (%)	Treated area (mm^2)
1.0 mm	8.1 ± 2.9	5.3 ± 1.0	18.2 ± 2.1
2.0 mm	9.5 ± 3.4	5.8 ± 1.2	20.7 ± 2.5
3.0 mm	11.5 ± 4.0	6.6 ± 1.4	23.0 ± 2.9

Figure 10 strengthens the claims of Table 2 with the observation that, as the degree of cone eccentricity increases, so do both residual deficit and treated area. This is consis-

tent from a clinical standpoint, as eccentric problems require increased safety-conscious treatment footprints.

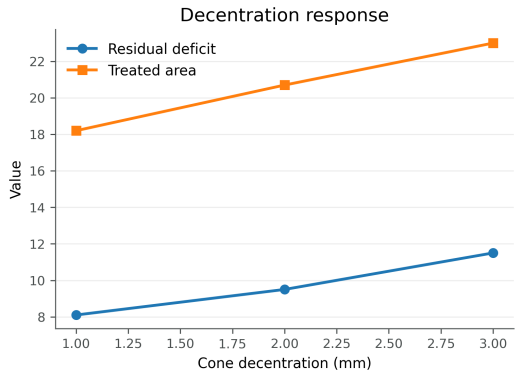

Figure 10. Decentration response.

3.5. Spatial and Longitudinal Dynamics

The longitudinal dynamics are represented by Figures 11–14. Each trajectory is shown in separate plots to keep numbers readable, while the corneal records are included in a consolidated figure panel. As before, the rankings are preserved in all graphs, with MO-CXL leading in each of them.

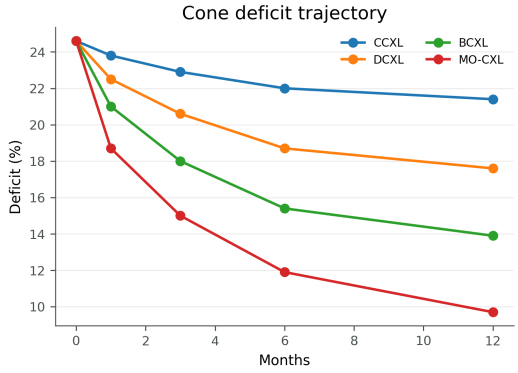

Figure 11. Cone deficit over time.

Figure 11 shows that the optimized protocol separates early from the comparator curves and maintains the lowest residual deficit through 12 months in the simulated follow-up.

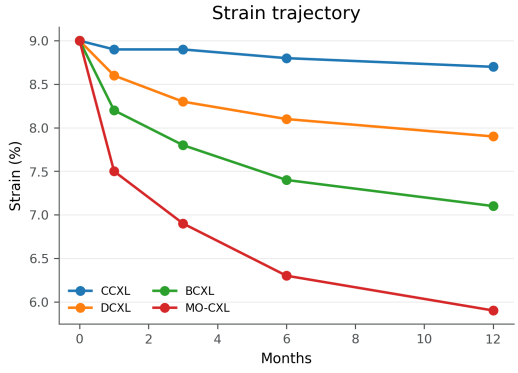

Figure 12. Strain over time.

Figure 12 indicates that the lower post-treatment strain is sustained rather than being a single endpoint artifact. Figure 13 shows the benefit of including curvature disturbance in the objective function. MO-CXL has the lowest cumulative curvature change among the four protocol families. Figure 14 suggests that optical regularity is best preserved when reinforcement is placed in proportion to the material deficit rather than imposed as a broad or fixed template.

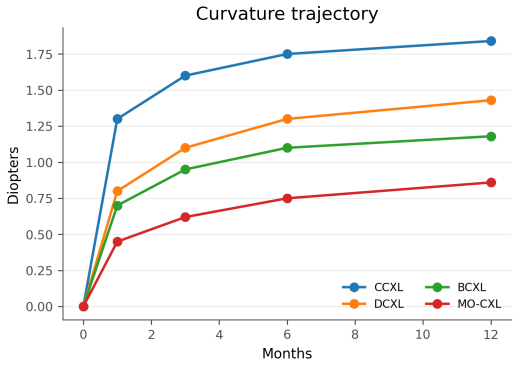

Figure 13. Curvature change over time.

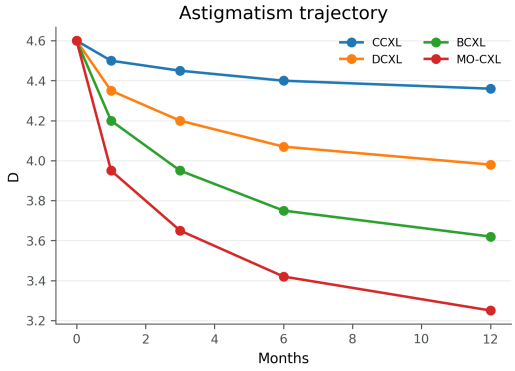

Figure 14. Astigmatism over time.

4. Discussion

The results of the present study show that the residual stiffness deficit mapped in a regional SSI can be utilized as a design objective for customized CXL treatments. This conclusion is relevant since the development of corneal biomechanics has been mainly concerned with improving ectatic defect localization and detection. The current study used this capability to optimize the distribution of the treatment intensity.

The maximum improvement was found to be associated with MO-CXL in comparison with standard centered treatment, where CCXL was the least successful option. CCXL provided the widest field of treatment but had the largest remaining cone deficit and cone curvature. MO-CXL minimized these metrics, thus proving the importance of spatial treatment optimization. MO-CXL was able to achieve this goal by adjusting its footprint to the deficit and safety requirements.

Comparing MO-CXL with DCXL and BCXL is also insightful. Both rule-based customization techniques proved to be superior to CCXL. However, neither of them was capable of surpassing the MO-CXL results. DCXL failed to adjust its footprint due to the circular treatment geometry, and BCXL was restricted by the fixed symmetric treatment pattern. MO-CXL provided higher flexibility by adjusting the location, shape, taper, and effective area of the footprint in accordance with the deficit and safety information.

Another important result is connected with strain reduction. The curvature reduction allows for assessing the visual benefit of CXL, but the strain reduction can help evaluate the

efficacy from the standpoint of preventing further progressive deformation. A cornea can become visually better but mechanically unstable due to residual strain accumulation. The MO-CXL treatment reduced peak strain in the cone area from $8.7 \pm 1.9\%$ with CCXL to $5.9 \pm 1.3\%$. Hence, MO-CXL was able to move the cornea towards a more stable configuration without changing the stress loading.

Optimization of curvature proved to be relevant for designing the multi-objective strategy. While maximizing the stiffness may lead to overcurving the cornea, the minimization of shape change will provide a weakly reinforced cornea. In such a case, both results need to be balanced. This goal was reached in MO-CXL with minimizing the treatment-induced curvature change and maximizing the stiffness increase.

The treated area turned out to be small in all MO-CXL cases, which is important despite the fact that no epithelium healing, endothelial cell damage, pain, haze, oxygen dynamics, or wound biology were taken into account in the current study. Such a treatment pattern is desirable in the design framework since it indicates a rational usage of the CXL dose. The value of compactness is also dependent on the concomitant improvement of strain and deficit parameters, which happened in the current sample.

The current study had several limitations. First, the sample was hypothetical and simulated. Second, the material constitutive model assumed the phenomenological form of the energy density law. Third, the treatment response parameters were obtained from existing literature and required a specific prospective study. Finally, the finite element approach used to simulate depth-dependent cross-linking, hydration, oxygen diffusion, epithelium status, and collagen structure simplifies the process. SSI-based input fields were considered as predefined while their measurement, registration, and uncertainty handling remain challenges in clinical application. Nonetheless, this does not undermine the relevance of the optimization findings.

Further research needs to involve actual patients, clinical imaging techniques, patient-specific depth-dependent energy transport, uncertainty-based computation of the SSI map, and prospectively evaluated treatment response parameters. The final result is expected to allow for calculating and reporting MO-CXL footprints with confidence intervals. It will also be necessary to assess whether the treatment design can be applied in the presence of safety-related constraints on the footprint.

5. Conclusion

The research hypothesis stated that regional stiffness-deficit maps could be used for calculating custom CXL patterns that would provide superior performance compared to standard and rule-driven geometries. According to the results obtained from a 48-eye virtual cohort, the map-driven CXL pattern showed the best performance among all other approaches tested, offering minimum cone deficit, minimum peak strain on the cone, the least RMS distortion of corneal curvature and the smallest treated area while still providing adequate safety margins.

Thus, the research conclusion cannot be viewed merely as an abstract assertion that customizing treatment is beneficial. It should be specified in relation to the particular approach applied to achieve such customization, namely using the regional SSI-derived defect map as input for the biomechanical optimization procedure that determines the optimal shape of the CXL pattern. This reinforces the core concept that the planning of keratoconus therapy should take into account not only the geometry but also the spatial arrangement of material vulnerability.

References

[1] Rabinowitz, Y. S. (1998). Keratoconus. Survey of Ophthalmology, 42(4), 297–319.

[2] Romero-Jimenez, M., Santodomingo-Rubido, J., & Wolffsohn, J. S. (2010). Keratoconus: a review. Contact Lens and Anterior Eye, 33(4), 157–166.

[3] Gomes, J. A., Tan, D., Rapuano, C. J., Belin, M. W., Ambrosio Jr, R., Guell, J. L., Malecaze, F., Nishida, K., Sangwan, V. S., & Group of Panelists for the Global Delphi Panel of Keratoconus and Ectatic Diseases. (2015). Global consensus on keratoconus and ectatic diseases. Cornea, 34(4), 359–369.

[4] Meek, K. M., & Knupp, C. (2015). Corneal structure and transparency. Progress in Retinal and Eye Research, 49, 1–16.
[5] Dupps, W. J. (2005). Biomechanical modeling of corneal ectasia. Journal of Refractive Surgery, 21(2), 186–190.
[6] Carvalho, L. A., Prado, M., Cunha, R. H., Costa Neto, A., Paranhos Jr, A., Schor, P., & Chamon, W. (2009). Keratoconus prediction using a finite element model of the cornea with local biomechanical properties. Arquivos Brasileiros de Oftalmologia, 72, 139–145.
[7] Roberts, C. J., & Dupps Jr, W. J. (2014). Biomechanics of corneal ectasia and biomechanical treatments. Journal of Cataract & Refractive Surgery, 40(6), 991–998.
[8] Spoerl, E., Huhle, M., & Seiler, T. (1998). Induction of cross-links in corneal tissue. Experimental Eye Research, 66(1), 97–103.
[9] Wollensak, G., Spoerl, E., & Seiler, T. (2003). Riboflavin/ultraviolet-A-induced collagen crosslinking for the treatment of keratoconus. American Journal of Ophthalmology, 135(5), 620–627.
[10] Caporossi, A., Baiocchi, S., Mazzotta, C., Traversi, C., & Caporossi, T. (2006). Parasurgical therapy for keratoconus by riboflavin-ultraviolet type A rays induced cross-linking of corneal collagen. Journal of Cataract & Refractive Surgery, 32(5), 837–845.
[11] Raiskup-Wolf, F., Hoyer, A., Spoerl, E., & Pillunat, L. E. (2008). Collagen crosslinking with riboflavin and ultraviolet-A light in keratoconus: long-term results. Journal of Cataract & Refractive Surgery, 34(5), 796–801.
[12] Koller, T., Mrochen, M., & Seiler, T. (2009). Complication and failure rates after corneal crosslinking. Journal of Cataract & Refractive Surgery, 35(8), 1358–1362.
[13] Raiskup, F., & Spoerl, E. (2013). Corneal crosslinking with riboflavin and ultraviolet-A. Part II. Clinical indications and results. The Ocular Surface, 11(2), 93–108.
[14] O'Brart, D. P. S. (2014). Corneal collagen cross-linking: a review. Journal of Optometry, 7(3), 113–124.
[15] Raiskup, F., Theuring, A., Pillunat, L. E., & Spoerl, E. (2015). Corneal collagen crosslinking with riboflavin and ultraviolet-A light in progressive keratoconus: ten-year results. Journal of Cataract & Refractive Surgery, 41(1), 41–46.
[16] Kanellopoulos, A. J., Dupps, W. J., Seven, I., & Asimellis, G. (2014). Toric topographically customized transepithelial, pulsed, very high-fluence, higher energy and higher riboflavin concentration collagen cross-linking in keratoconus. Case Reports in Ophthalmology, 5(2), 172–180.
[17] Seiler, T. G., Fischinger, I., Koller, T., Zapp, D., Frueh, B. E., & Seiler, T. (2016). Customized corneal cross-linking: one-year results. American Journal of Ophthalmology, 166, 14–21.
[18] Cassagne, M., Pierne, K., Galiacy, S. D., Asfaux-Marfaing, M. P., Fournie, P., & Malecaze, F. (2017). Customized topography-guided corneal collagen cross-linking for keratoconus. Journal of Refractive Surgery, 33(5), 290–297.
[19] Luce, D. A. (2005). Determining in vivo biomechanical properties of the cornea with an ocular response analyzer. Journal of Cataract & Refractive Surgery, 31(1), 156–162.
[20] Ortiz, D., Pinero, D., Shabayek, M. H., Arnalich-Montiel, F., & Alio, J. L. (2007). Corneal biomechanical properties in normal, post-LASIK, and keratoconic eyes. Journal of Cataract & Refractive Surgery, 33(8), 1371–1375.
[21] Fontes, B. M., Ambrosio Jr, R., Velarde, G. C., & Nose, W. (2011). Ocular response analyzer measurements in keratoconus with normal central corneal thickness compared with matched normal control eyes. Journal of Refractive Surgery, 27(3), 209–215.
[22] Vinciguerra, R., Ambrosio Jr, R., Elsheikh, A., Roberts, C. J., Lopes, B., Morenghi, E., Azzolini, C., & Vinciguerra, P. (2016). Detection of keratoconus with a new biomechanical index. Journal of Refractive Surgery, 32(12), 803–810.
[23] Vinciguerra, R., Ambrosio Jr, R., Roberts, C. J., Azzolini, C., & Vinciguerra, P. (2017). Biomechanical characterization of subclinical keratoconus without topographic or tomographic abnormalities. Journal of Refractive Surgery, 33(6), 399–407.
[24] Ambrosio Jr, R., Lopes, B. T., Faria-Correia, F., Salomao, M. Q., Buhren, J., Roberts, C. J., Elsheikh, A., Vinciguerra, R., Vinciguerra, P., & Belin, M. W. (2017). Integration of Scheimpflug-based corneal tomography and biomechanical assessments for enhancing ectasia detection. Journal of Refractive Surgery, 33(7), 434–443.
[25] Ferreira-Mendes, J., Lopes, B. T., Faria-Correia, F., Salomao, M. Q., Rodrigues-Barros, S., & Ambrosio Jr, R. (2019). Enhanced ectasia detection using corneal tomography and biomechanics. American Journal of Ophthalmology, 197, 7–16.
[26] Eliasy, A., Chen, K. J., Vinciguerra, R., Lopes, B. T., Abass, A., Vinciguerra, P., Ambrósio Jr, R., Roberts, C. J., & Elsheikh, A. (2019). Determination of corneal biomechanical behavior in vivo for healthy eyes using CorVis ST tonometry: stress-strain index. Frontiers in Bioengineering and Biotechnology, 7, 105.
[27] Zhang, H., Eliasy, A., Lopes, B., Abass, A., Vinciguerra, R., Vinciguerra, P., Ambrosio Jr, R., Roberts, C. J., & Elsheikh, A. (2021). Stress-strain index map: a new way to represent corneal material stiffness. Frontiers in Bioengineering and Biotechnology, 9, 640434.